

Compression and Reconstruction of Random Microstructures using Accelerated Lineal Path Function

Jan Havelka^a, Anna Kučerová^{a,*}, Jan Sýkora^a

^a*Department of Mechanics, Faculty of Civil Engineering, Czech Technical University in Prague, Thákurova 7, 166 29 Prague 6, Czech Republic*

Abstract

Microstructure reconstruction and compression techniques are designed to find a microstructure with desired properties. While the microstructure reconstruction searches for a microstructure with prescribed statistical properties, the microstructure compression focuses on efficient representation of material morphology for a purpose of multiscale modelling. Successful application of those techniques, nevertheless, requires proper understanding of underlying statistical descriptors quantifying material morphology. In this paper we focus on the lineal path function designed to capture namely short-range effects and phase connectedness, which can be hardly handled by the commonly used two-point probability function. The usage of the lineal path function is, however, significantly limited by huge computational requirements. So as to examine the properties of the lineal path function within the computationally exhaustive compression and reconstruction processes, we start with the acceleration of the lineal path evaluation, namely by porting part of its code to the graphics processing unit using the CUDA (Compute Unified Device Architecture) programming environment. This allows us to present a unique comparison of the entire lineal path function with the commonly used rough approximation based on the Monte Carlo and/or sampling template. Moreover, the accelerated version of the lineal path function is then compared with the two-point probability function within the compression and reconstruction of two-phase morphologies. Their significant features are thoroughly discussed and illustrated on a set of artificial periodic as well

*Corresponding author. Tel.: +420-2-2435-5326; fax +420-2-2431-0775

Email addresses: `jan.havelka.1@fsv.cvut.cz` (Jan Havelka),
`anicka@cml.fsv.cvut.cz` (Anna Kučerová), `jan.sykora.1@fsv.cvut.cz` (Jan Sýkora)

as real-world random microstructures.

Keywords: Lineal path function, Two-point probability function, Statistically equivalent periodic unit cell, Microstructure reconstruction, Microstructure compression, Graphics processing unit, Compute Unified Device Architecture

1. Introduction

Computational modelling of random heterogeneous materials is a non-trivial multi-disciplinary problem with a wide range of relevant engineering applications. The FE^2 -methods have been developed as promising techniques for material modelling and used to derive effective models at the scale of interest. The unifying theoretical framework is provided by homogenization theories aiming at the replacement of the heterogeneous microstructure by an equivalent homogeneous material, see [1]. Currently, two main approaches are available: (i) computational homogenization and (ii) effective media theories.

The latter approach aims at estimating the material response analytically on the basis of limited geometrical information (e.g. the volume fractions of constituents) of the analysed medium. Structural imperfections are introduced in a cumulative sense using one of the averaging schemes, e.g. the Mori-Tanaka method [2]. The computational requirements are very low, however, such an analytical solution is available only for a limited spectrum of microstructural geometries such as media with a specific shape of inclusions.

Methods based on computational homogenization are more general in application. They study the distribution of local fields within a typical heterogeneity pattern using a numerical method. It is generally accepted that detailed discretisation techniques, and the finite element method in particular, remain the most powerful and flexible tools available. Despite the tedious computational time, it provides us the details of local fields, see e.g. [3, 4]. However, the principal requirement is to find a representative volume element (RVE), which can be intriguing in case of real-world random microstructures. Recent studies [5, 6] suggest that structure preserving spatial geometrical statistics such as a statistically equivalent periodic unit cell (SEPUC) – also known as a statistically similar representative volume element (SSRVE) – is computationally very efficient comparing to the classical concept of the RVE.

A relatively new concept of microstructure modelling is based on the

production of a set of structures morphologically similar to the original media, so called Wang tiles, see [7, 8]. It is an approach that allows us to obtain aperiodic local fields in heterogeneous media with a small set of statistically representative tiles. The main advantage of the stochastic Wang tilings is the computational efficiency and long range spatial correlations, which are neglected in classical homogenization techniques, see [7]. The tiles can be in some cases produced by a computational efficient image quilting algorithm [9] or generally also by optimising a chosen statistical descriptor.

The present paper is devoted to statistical descriptors defining statistically/morphologically similar material structures (cells or tiles). Such structures are generally obtained by a process of microstructure reconstruction [10] or compression [11] so as to represent the microstructure as accurately as possible in terms of the selected statistical descriptor. In particular, we focus on two commonly used descriptors, the two-point probability function and the lineal path function, see [12, 13, 6]. The goal of this paper is to investigate in more detail the properties and differences of these two descriptors within the compression and reconstruction process. So as to achieve this goal, we concentrate on calculation of the entire lineal path function instead of its often used rough discretisation by a sampling template evaluated approximately using a Monte Carlo-based procedure, see [14]. Since the evaluation of the entire lineal path function can be computationally extremely exhaustive, we present certain acceleration steps on the algorithmic as well as on the implementation side, where the significant speed up is achieved namely by porting the algorithm to the graphics processing unit (GPU) using the CUDA environment.

This article has been organised in the following way. The next section describes a theoretical formulation of the both descriptors. Section 3 is devoted to acceleration of the lineal path function and presents the resulting speed-up obtained at GPU in comparison with the sequential CPU formulation. Section 4 briefly introduces the optimisation algorithm employed for microstructure compression and reconstruction discussed in Sections 5 and 6, respectively. Final summary of the essential findings are provided in Section 7.

2. Statistical description of random media

The morphology quantification for random heterogeneous materials starts from the introduction of the concept of an ensemble established by Kröner [15]

and Beran [16]. Proposed mathematical formulations are considered as one of the milestones in statistical physics and the basic idea is that macroscopic observables can be calculated by performing averages over the systems in the ensemble. In other words, the ensemble represents the collection of geometrical systems having different microstructures but being completely identical from a macroscopic point of view [14].

A variety of statistical descriptors were developed to describe the morphology of a multi-phase random heterogenous material [14, 5] based on the concept of an ensemble. In the present work, the two-point probability function and the lineal path function are investigated as frequently used descriptors. Therefore, this section provides their brief analytical description and classical numerical implementation.

As a preamble, throughout this paper we consider an ensemble of a two-phase medium consisting of a black and white phase labelled by superscripts $i, j \in \{b, w\}$. We also model the medium only as a two-dimensional system, where the position of an arbitrary point \mathbf{x}_a is defined by the Cartesian coordinates $\mathbf{x}_a = (x_a, y_a)$. Nevertheless, the extension into the three-dimensional systems is very straightforward.

2.1. Two-point probability function

More formally, the two-point probability function $S_2^{ij}(\mathbf{x}_1, \mathbf{x}_2)$ ¹ quantifies the probability of finding simultaneously the phase i and the phase j at two arbitrarily chosen points \mathbf{x}_1 and \mathbf{x}_2 , respectively, and can be written in the form, see [14, 17],

$$S_2^{ij}(\mathbf{x}_1, \mathbf{x}_2) = \langle \chi^i(\mathbf{x}_1, \alpha) \chi^j(\mathbf{x}_2, \alpha) \rangle, \quad (1)$$

where the symbol $\langle \cdot \rangle$ denotes the ensemble average of the product of characteristic functions $\chi^i(\mathbf{x}_a, \alpha)$, which are equal to one when the point \mathbf{x}_a lies in the phase i in the sample α and equal to zero otherwise:

$$\chi^i(\mathbf{x}_a, \alpha) = \begin{cases} 1, & \text{if } \mathbf{x}_a \in D^i(\alpha) \\ 0, & \text{otherwise} \end{cases}. \quad (2)$$

In Eq. (2), $D^i(\alpha)$ denotes the domain occupied by the i -th phase. In general, the evaluation of these characteristics may prove to be prohibitively

¹with S_2^i abbreviating S_2^{ii}

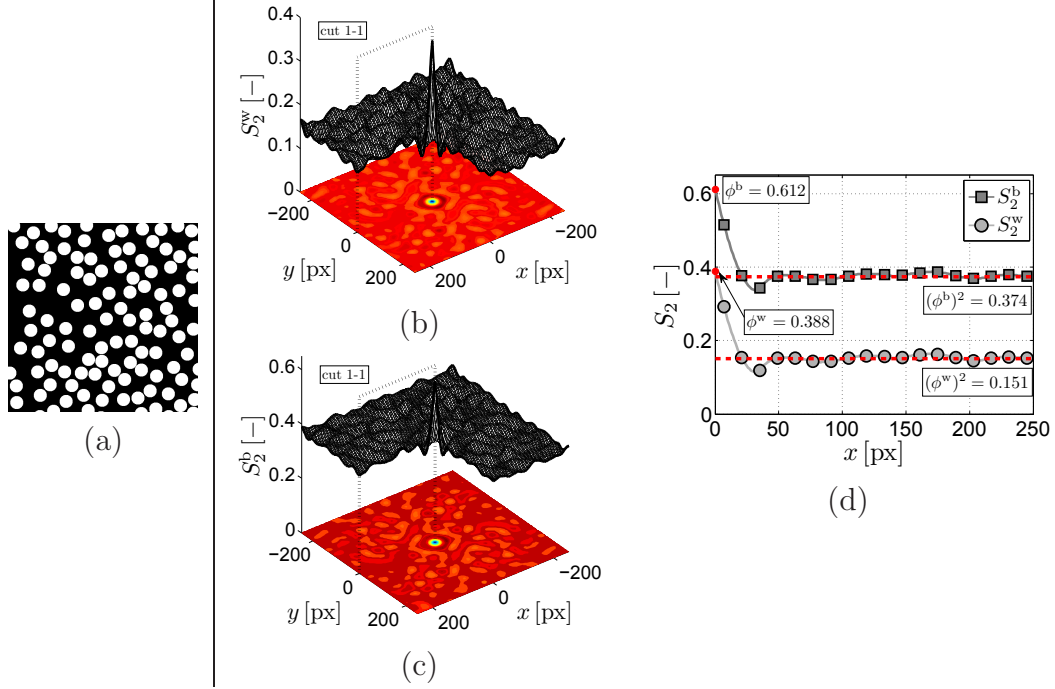


Figure 1: Illustration of the two-point probability function: (a) Example of a homogeneous system, size 500×500 [px]; (b) S_2^w -function; (c) S_2^b -function; (d) Comparison of S_2 -functions in cut 1-1.

difficult. Fortunately for homogeneous systems, the S_2^i depends only on the relative position of the two points $\mathbf{x} = \mathbf{x}_2 - \mathbf{x}_1$ and has following asymptotic properties, see [10],

$$S_2^i(|\mathbf{x}| = 0) = \phi^i, \quad (3)$$

$$\lim_{|\mathbf{x}| \rightarrow \infty} S_2^i(\mathbf{x}) = (\phi^i)^2, \quad (4)$$

where ϕ^i is the volume fraction of the i -th phase. Eq. (3) follows from definition (1) and means that the probability of a randomly thrown point (i.e. vector of zero length) falling into the phase i is equal to the volume fraction of the phase i . On the other hand, Eq. (4) assumes that the system has no long-range correlations and thus, falling of the two distant points \mathbf{x}_1 and \mathbf{x}_2 into the phase i are independent events, each having the probability equal to ϕ^i , see Fig. 1 as an illustrative example of such a system.

Even though we aim at characterization of generally non-periodic media by a SEPUC, whose boundaries are constructed as periodic, it has been

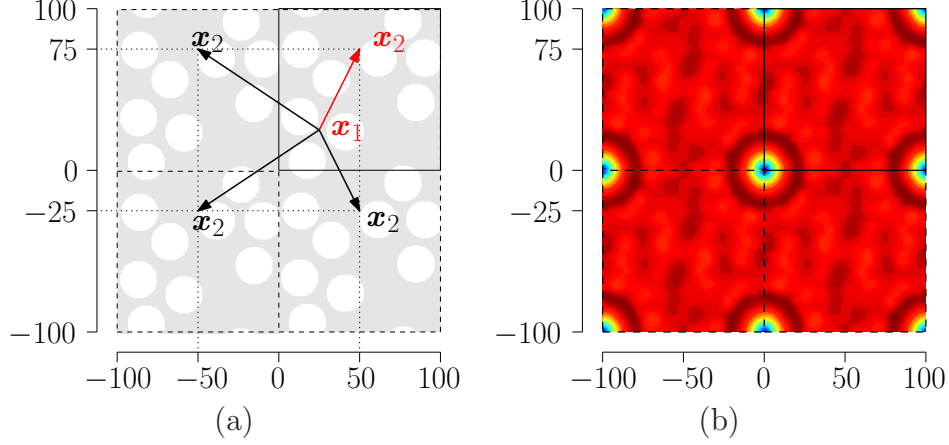


Figure 2: Vectors connecting identical points in periodical setting (a) and the corresponding identical values of the periodic two-point probability function (b)

demonstrated in [18] that assumption of periodic boundaries does not introduce a systematic bias in the values of statistical descriptors. On the other hand, the assumption of the periodicity simplifies the computation of the two-point probability function, because we do not need to consider all the possible orientations of the vector \mathbf{x} . As shown in Fig. 2a, four differently oriented vectors are actually connecting the identical points and obviously have the same value of the two-point probability function. As a consequence, the evaluation of the two-point probability function for vectors oriented into the first quadrant includes the information about all the other vector orientations, see Fig. 2b.

The last note concerns particularly the two-phase medium, where the two-point probability functions of particular phases are related according to the following equation

$$S_2^i(\mathbf{x}) = (\phi^i)^2 - (\phi^j)^2 + S_2^j(\mathbf{x}), \quad (5)$$

i.e. they differ only by a constant as also visible in Fig. 1d. Since the constant is given by known volume fractions of particular phases, only one two-point probability function needs to be determined to describe the two-phase medium. For this reason, we may drop the superscript of $S_2^i(\mathbf{x})$ and write only the two-point probability function as $S_2(\mathbf{x})$.

Implementation of the two-point probability function is based on the assumption of a discrete description of a studied system, mainly binary images

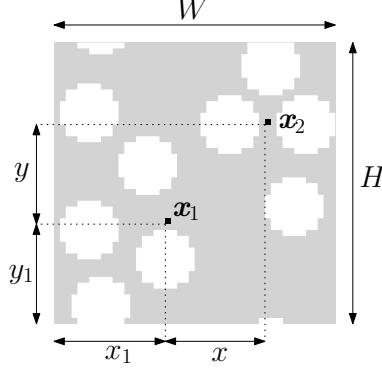


Figure 3: Illustration of a digitised image

in our case. The general and simple Monte Carlo-based evaluation strategy throws randomly two points into the investigated medium and counts successful “hits” of both points into the phase i . This approach is, however, not only approximate, but also very computationally demanding. Therefore, another practical method was introduced on the basis of rewriting the two-point probability function as an autocorrelation of the characteristic function χ^i for a periodic medium as, see [14],

$$S_2^i(x, y) = \frac{1}{WH} \sum_{x_1=0}^{W-1} \sum_{y_1=0}^{H-1} \chi^i(x_1, y_1) \chi^i((x_1 + x) \% W, (y_1 + y) \% H), \quad (6)$$

where the symbol $\%$ is the modulo, $\chi^i(x_1, y_1)$ denotes the value of χ^i for the pixel located in the y_1 -th row and the x_1 -th column of the digitised image with the dimensions $W \times H$, x and y are the vertical and horizontal distances between two pixels, see Fig. 3. According to [17], the Eq. (6) can be computed in an efficient way using the Fast Fourier Transform. Applying this, the reformulation of the two-point probability function S_2^i for a periodic medium can be written as

$$S_2^i(x, y) = \frac{1}{WH} \text{IDFT} \left\{ \text{DFT} \{ \chi^i(x, y) \} \overline{\text{DFT} \{ \chi^i(x, y) \}} \right\}, \quad (7)$$

where IDFT is the inverse Discrete Fourier Transform (DFT), the symbol $\bar{\cdot}$ stands for the complex conjugate. This method is very efficient and its accuracy depends only on the selected resolution of the digitised medium, see [14, 5]. The Fast Fourier Transform, which needs only $\mathcal{O}(WH \log(WH) + WH)$ operations, is used to perform the numerical computations presented below.

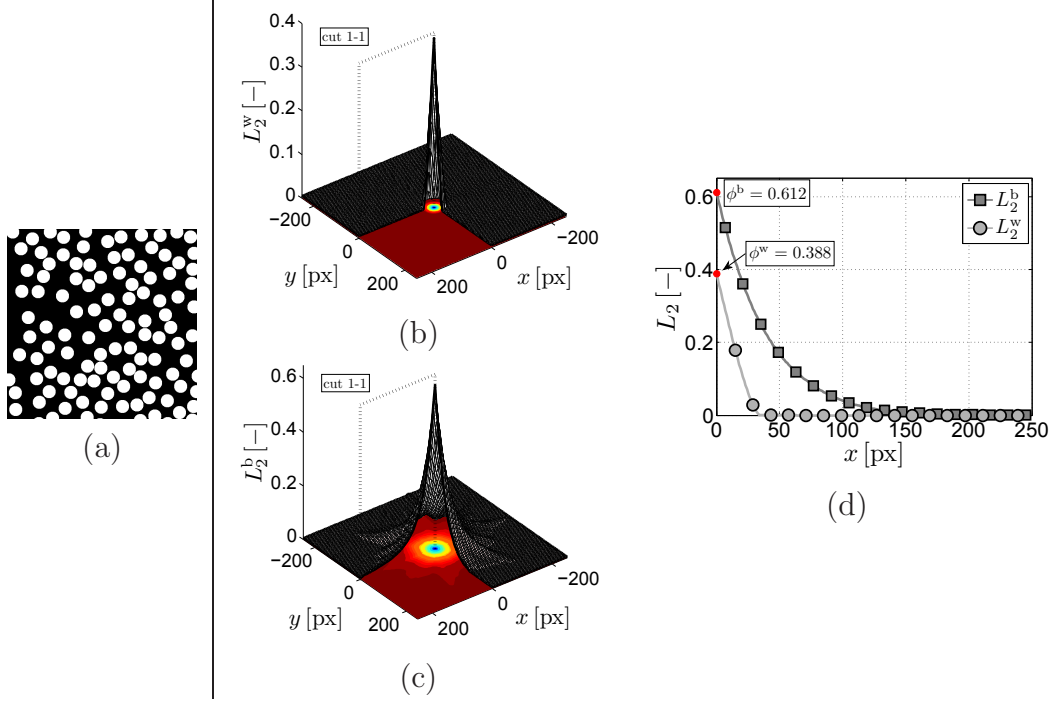


Figure 4: Illustration of the two-point probability function: (a) Example of a homogeneous system, size 500×500 [px]; (b) L_2^w -function; (c) L_2^b -function; (d) Comparison of L_2 -functions in cut 1-1.

2.2. Lineal path function

Another frequently used statistical descriptor for the microstructural morphology quantification is the lineal path function $L_2^i(\mathbf{x}_1, \mathbf{x}_2)$, originally introduced in [19] and further elaborated in [10, 14]. It is defined as a low-order descriptor based on a more complex fundamental function λ^i able to describe certain information about the phase connectedness and putting more emphasis on the short-range correlations, since its value quickly vanishes to zero with increasing $|\mathbf{x}|$. The fundamental function λ^i is defined as

$$\lambda^i(\mathbf{x}_1, \mathbf{x}_2, \alpha) = \begin{cases} 1, & \text{if } \mathbf{x}_1\mathbf{x}_2 \subset D^i(\alpha), \\ 0, & \text{otherwise,} \end{cases} \quad (8)$$

i.e., a function which equals to 1 when the segment $\mathbf{x}_1\mathbf{x}_2$ is contained in the phase i for the sample α and 0 otherwise. The lineal path function is defined as the probability that the line segment $\mathbf{x}_1\mathbf{x}_2$ lies entirely in the phase i and

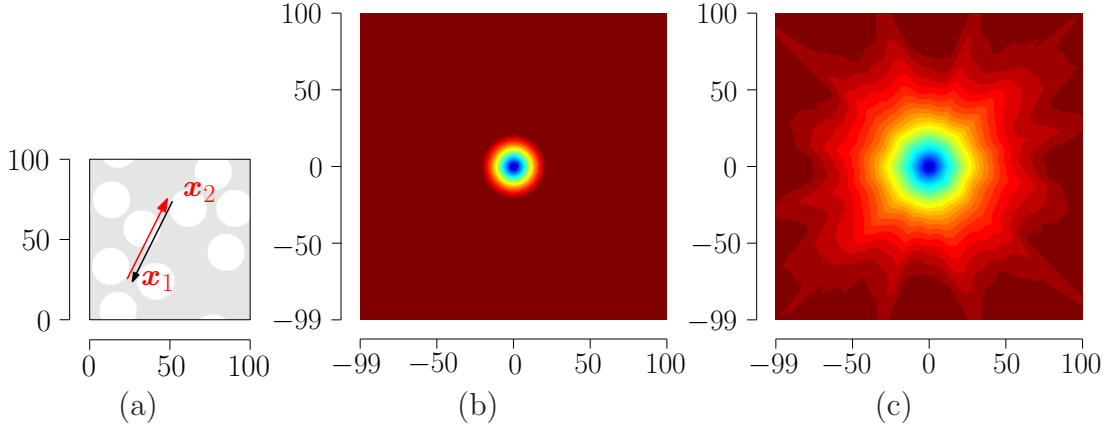


Figure 5: Vectors corresponding to identical segments (a), point symmetry of lineal path function of the black (b) and white (c) phases

it can be written as the ensemble averaging fundamental function given as

$$L_2^i(\mathbf{x}_1, \mathbf{x}_2) = \langle \lambda^i(\mathbf{x}_1, \mathbf{x}_2, \alpha) \rangle. \quad (9)$$

As mentioned above, under the assumption of statistical homogeneity [14], the function again simplifies to $L_2^i(\mathbf{x}_1, \mathbf{x}_2) = L_2^i(\mathbf{x})$ with $\mathbf{x} = \mathbf{x}_2 - \mathbf{x}_1$ and yields

$$L_2^i(|\mathbf{x}| = 0) = \phi^i \quad (10)$$

$$\lim_{|\mathbf{x}| \rightarrow \infty} L_2^i(\mathbf{x}) = 0. \quad (11)$$

Here again, the Eq. 11 assumes no long-range correlations and thus the probability that the line segment $\mathbf{x}_1\mathbf{x}_2$ lies entirely in the phase i vanishes to zero with its increasing length, see Fig. 4 for an illustration of such a homogeneous system.

For the sake of consistency with the formulation and computation of the two-point probability function, we introduce again the assumption of the periodicity in our numerical implementation. However, there arise no computational benefits, since all the vectors in Fig. 2a are connecting the same points via a different path. Nevertheless, we need to keep in mind that the line segment $\mathbf{x}_1\mathbf{x}_2$ is identical to the line segment $\mathbf{x}_2\mathbf{x}_1$ and thus

$$L_2^i(\mathbf{x}) = L_2^i(-\mathbf{x}), \quad (12)$$

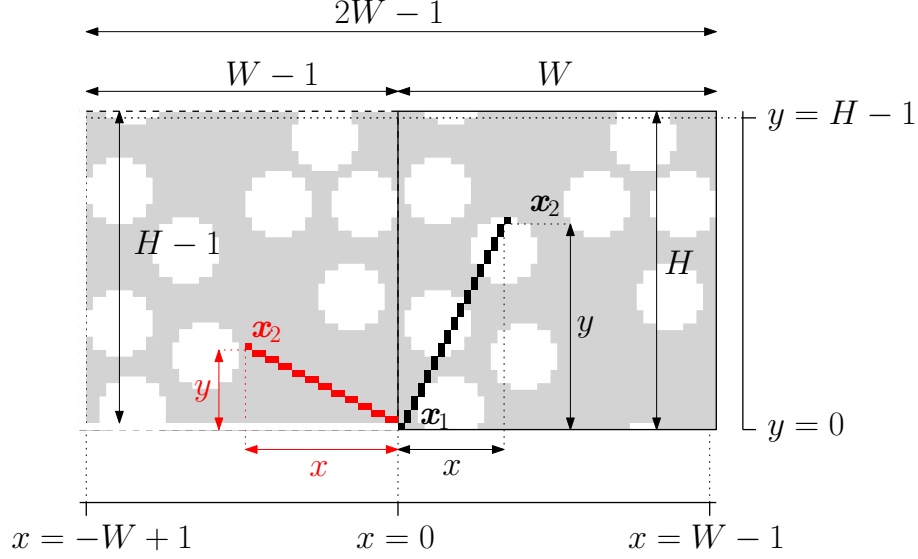


Figure 6: Illustration of line segments

which means that the lineal path possesses point symmetry, see Fig. 5. Hence, we need to compute the lineal path function only for a half of all the possible orientations of the vector \mathbf{x} and the rest is obtained by symmetry.

In contrast to the evaluation of S_2^i , see Eq. (5), the lineal path function computed for one phase does not include the whole information about the lineal path function of the other phase, which thus needs to be computed separately, see Fig. 5. This brings additional information about the structural morphology, but it also means higher computational demands.

With this in mind, the standard numerical implementation of a sequential version of the entire L_2^i starts from the definition of line segments connecting two pixels \mathbf{x}_1 and \mathbf{x}_2 within the image with the dimensions $W \times H$. The set of pixels representing a segment starting in $\mathbf{x}_1 = (0, 0)$ and ending in $\mathbf{x}_2 = (x, y)$, is specified by an algorithm originally proposed by Bresenham [20] defining a unique solution for any positions of boundary pixels $\mathbf{x}_1, \mathbf{x}_2$. Due to the point symmetry of the lineal path function, all the orientations of a line segment necessary for its computation are produced by moving the point \mathbf{x}_2 within the domain \mathbb{D} given by two rectangles specifying the left bottom corner of a pixel, i.e.

$$\mathbb{D} := [-W + 1; -1] \times [1; H - 1] + [0; W - 1] \times [0; H - 1] \quad (13)$$

see Fig. 6. The number of segments defining the lineal path function is thus given as a cardinality of the domain \mathbb{D} , which is $|\mathbb{D}| = 2HW - H - W + 1$. Once having the defined segments, the computation of the lineal path function involves simple translations of each segment throughout the image and the comparison whether all pixels of the segment at a given position correspond to image pixels with the value of the investigated phase. Such an intuitive description represents, however, a computationally exhaustive procedure leading to $\mathcal{O}(H^3W^2)$ operations for periodic media with $W \leq H$. For our purpose, it simplifies to $\mathcal{O}(W^5)$ for $W = H$, i.e. a square shape of SEPUC/SSRVE. In order to reduce the computational cost, several algorithmic and hardware acceleration steps are introduced and described in the following section.

3. Numerical implementation of L_2

In order to avoid huge computational requirements of the entire L_2 evaluation, some authors (see e.g. [14]) compute only its approximation using a Monte Carlo-based procedure. In such a case, the line segments are not compared with the image at all available positions equal to a number of all pixels in the image, but only at a limited number of randomly selected positions. The error produced by such an approximation is illustrated in Figure 7 for three different types of microstructures as a function of the number N of selected positions. The values on the vertical axis are the least square errors between the exact lineal path function L_2 and its approximation \tilde{L}_2 given as

$$e(L_2^i) = \sum_{p \in \mathbb{D}} (L_2^i(\mathbf{x}_p) - \tilde{L}_2^i(\mathbf{x}_p))^2, \quad (14)$$

where the superscript i denotes the phase and the subscript p covers all the oriented segments defining the lineal path function given by (13). Dimensions of all three microstructural images are 100×100 pixels. Since the lineal path function is evaluated at N positions obtained as a random N -combination of a set $|\mathbb{D}|$ without repetition, the error converges to zero for $N = |\mathbb{D}|$.

3.1. Parallelisation on GPU using CUDA environment

The key idea described here is a porting part of the code to GPU device. Parallel computations on GPUs have become very popular within the last decade thanks to the GPU's high performance at a relatively low financial

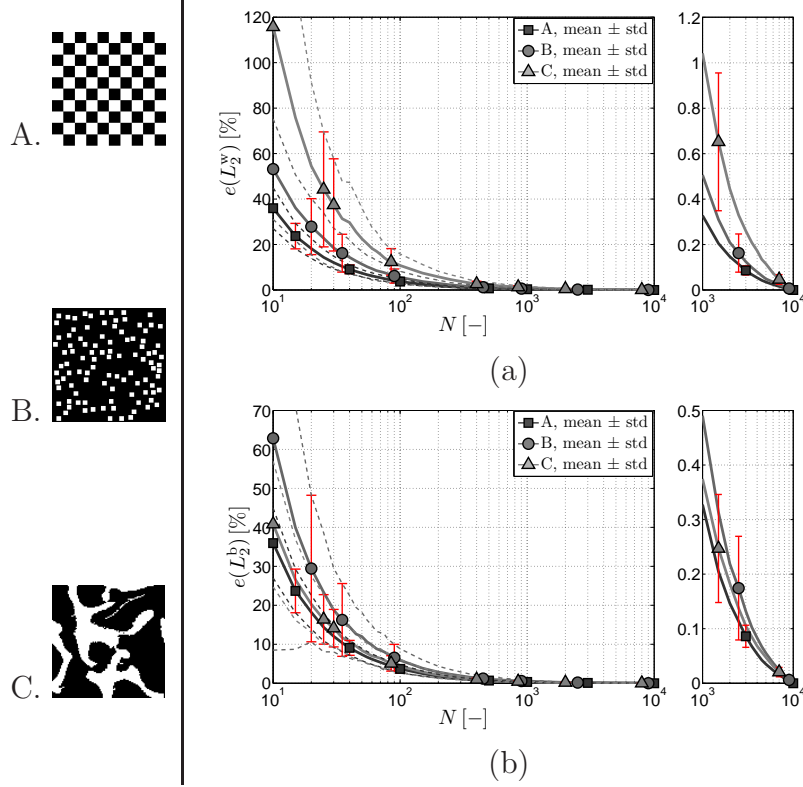


Figure 7: Convergence analysis of MC-based approximation of lineal path functions computed for (a) white phase and (b) black phase

cost. Moreover, the programming environment called CUDA (Compute Unified Device Architecture) simplifies the GPU-based software development by using the standard C/C++ language, see. [21]. In order to clearly describe the GPU parallelism, we start with the algorithmic structure of the L_2 evaluation consisting of several computational steps:

1. generating line segments for given input dimensions,
2. allocating the inputs (e.g. the input representing a binary image),
3. calculating the lineal path function based on translations of each segment and its comparison with the image.

Regarding computational requirements of particular steps, one needs to keep in mind that the L_2 is supposed to be called repeatedly within an optimisation process for new feasible solutions (i.e. new binary images) of

the same dimensions $W \times H$. It means that the definition of line segments remains the same during the whole optimisation process thus allowing to run the step 1 only once at the beginning of the optimisation, while the steps 2 – 3 need to be called repeatedly. It also further implies that step 1 is critical namely from the memory usage point of view, while steps 2 – 3 needs to be optimised with respect to the computational time.

Before starting an implementation of Bresenham's algorithm for definition of line segments, one needs to decide about the line segments coding. While the definition of a particular pixel by its (x, y) coordinates is very intuitive, it is excessively memory demanding. It is much more efficient to index all pixels in the image by only one integer value from 0 to $WH - 1$. Then the number of integer values required for definition of all line segments is given as

$$M = \sum_{i=1}^W \sum_{j=1}^H \max(i, j) + \sum_{i=2}^W \sum_{j=2}^H \max(i, j), \quad (15)$$

which leads to

$$M = \frac{W(3H^2 + 3H + W^2 - 1)}{3} - \frac{W(W + 1)}{2} - \frac{H(H + 1)}{2} + 1 \quad (16)$$

for $W \leq H$ and to

$$M = \frac{4W^3 - 4W + 3}{3} \quad (17)$$

for $H = W$. Figure 8 shows the dimensions of square images which can be handled by cards with a given memory size assuming that one integer takes 4 bytes.

As mentioned, the consecutive steps 2 and 3 are supposed to be called repeatedly within the optimisation process and thus represent the principal requirements on computational time, see Alg. 1 for a more detail algorithmic structure of the step 3. The image enters the algorithm as the matrix A twice wider and twice higher than the original one, because it is periodically copied on a grid 2×2 to allow easily translate the segments starting within the image and ensure the segments to never end outside the image. The translation is thus defined by moving the starting point of a segment within one quadrant of the entering image. To facilitate the repeatedly called computations, the indices of moves within one quadrant are precomputed and stored in the separate matrix C .

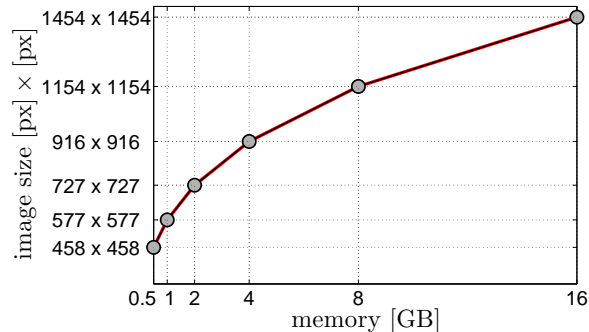


Figure 8: Illustration of memory requirements for line segments storage.

The structure of Alg. 1 suggests several ways of possible parallelisation. One way is a parallelisation over particular segments (line 1), which would, however, lead to a very asynchronous computation due to large differences among lengths of the segments. Parallelisation over translations (line 2) is not completely synchronous, because its inner cycle over pixels of the segment (line 3) is stopped when proceeds to a pixel which is not lying in a given phase, which depends on a particular image morphology. Nevertheless, the computation have at least a chance to be more synchronous than the surely highly asynchronous parallelisation over segments.

Fortunately, the algorithm clearly consists of a huge number of very simple logic and arithmetic operations and is thus well-suited for parallelisation on GPU because of following reasons:

- (i) It allows for a nearly synchronous parallelisation scheme thus respecting the basic GPU programming rule – memory coalescence;
- (ii) It corresponds to the SIMD (single instruction, multiple data) architecture: a single instruction is an index of segment to be compared with the image at all possible positions, which thus represents the multiple data;
- (iii) The most of the memory transfer corresponding to copying of image, translations, line segments and their sizes is done only once and in large chunks thus reducing related system overhead.

The parallel algorithmic structure proposed to increase the numerical efficiency of the L_2 computation is given in Alg. 2. The crucial step for

Data:

$A \dots$ a binary image defined as an integer vector of size $2W \cdot 2H$

$B \dots$ an irregular 2D integer matrix defining pixels of Bresenham's line segments of size $S \times \text{segment}$ size, where $S = 2WH - W - H + 1$

$C \dots$ an integer vector of size WH defining a translation within an image $W \times H$ mapped onto a periodically copied image of size $2W \times 2H$

$D \dots$ an integer vector of size S defining a size of particular segments

$phase \dots$ an integer defining phase, for which the L_2 is evaluated

Result: $L \dots$ an integer vector of size S defining the L_2

```

1 for  $seg=0$  to  $S - 1$  do
2   for  $transl=0$  to  $WH - 1$  do
3     for  $pix=0$  to  $D[seg]$  do
4       if  $A[B[seg][pix]+C[transl]] \neq phase$  then
5         break;
6       end
7     end
8     if  $pix = D[seg]$  then
9        $L[seg] = L[seg] + 1$ ;
10    end
11  end
12 end

```

Algorithm 1: Algorithmic structure of implementation designed for CPU device; seg , $transl$ and pix represent integer variables used to govern the corresponding for loops.

the implementation efficiency concerns line 9, where all $n_t = WH$ translations are distributed into available multiprocessors (MP). Since particular GPU architectures significantly differ among each other, here we concentrate on Fermi compute architecture [21], where each MP has 32 single-precision CUDA cores. It means that each MP can simultaneously solve up to 32 tasks – so-called threads – defining one warp. Besides currently computing threads, the MP can already load and prepare other threads up to maximally 1536 threads = 48 warps. The tasks are sent to the MP in blocks, where the particular translation is assigned to the particular thread automatically according to its position within the block. Storing the translations in a 1D

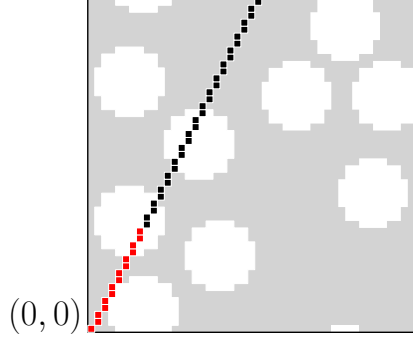


Figure 9: Illustration of overlapping line segments

vector instead of a 2D matrix thus allows for more even distribution of translations among the MPs. Each MP can handle at the same time maximally 8 blocks. Particular size of a block can be chosen by a programmer, but finding an optimum is not so straightforward. So as to maximise the occupancy of the MPs, it is convenient to define the size of block B as

$$B = \begin{cases} 1 \times 6 \text{ warps} = 1 \times 192 \text{ threads,} & \text{if } \left\lceil \frac{n_t}{n_{mp}} \right\rceil \geq 1536, \\ 1 \times \left\lceil \frac{n_t}{8n_{mp}} \right\rceil \text{ threads,} & \text{otherwise,} \end{cases} \quad (18)$$

where $\lceil \cdot \rceil$ denotes the round-up operation to the nearest integer and n_{mp} is a number of available MPs. Nevertheless, other aspects related to shared memory and registers [21] may move the preferences towards bigger blocks. More detailed study on the optimal block size is beyond the scope of this paper. In our computations, we focused on occupancy maximisation only and the block size is set according to Eq. (18).

3.2. Algorithmic acceleration of L_2 evaluation

Besides the parallelisation, we also propose one simple algorithmic acceleration of the lineal path computation. The idea comes from the discrete nature of segments and a fact that some shorter segments are overlapped by some longer segments. See Fig. 9, where all segments start at $\mathbf{x}_1 = (0, 0)$ and those ending in red pixels are overlapped by segments ending in black pixels. If a segment never falls entirely in a given phase and its L_2 value is zero, it is obvious that all longer overlapping segments will have the zero value as well. This simple logic brings additional significant time savings in the L_2


```

1 CPU:      calculating line segments: indices in  $B$  and sizes in  $D$ ;
2 CPU→GPU: copying  $B$  and  $D$  into GPU;
3 CPU:      loading and copying binary image onto grid  $2 \times 2$  saved
4            into  $A$ , defining translations  $C$  ;
5 CPU→GPU: copying  $C$  and  $phase$  into GPU;
6 CPU→GPU: copying  $A$  into GPU;
7 for  $seg = 0$  to  $S - 1$  do
8   CPU→GPU: copying  $seg$  into GPU;
9   GPU calls threads: for  $transl = 0$  to  $WH - 1$  do
10     $L[seg] = 0$ ;
11    for  $pix=0$  to  $D[seg]$  do
12     if  $A[B[seg][pix]+C[transl]] \neq phase$  then
13      break;
14     end
15    end
16    if  $pix = D[seg]$  then
17      $L[seg] = L[seg] + 1$ ;
18    end
19  end
20 end
21 CPU←GPU: copying  $L$  to CPU;

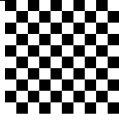
```

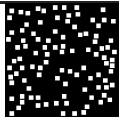
Algorithm 2: Simplified algorithmic structure of implementation designed for single GPU device; All variables are defined in Alg. 1.

evaluation. It only needs to precalculate a vector containing the indices of the longest shorter overlapping segments (LSOS). Such a precalculation is computational expensive, but is done only once at the beginning of the algorithm. Having in mind that steps 6 to 21 in Alg. 2 are supposed to be called repeatedly within an optimisation process, this precalculation should take place before step 3. Then one simple if-condition is added before translating and comparing the segments with the image. If the LSOS corresponding to the current segment has zero value of L_2 , then the L_2 value of the current segment is automatically assigned to zero value too and the translating and comparing phase is skipped. To be more specific, there are two possibilities where this crucial if-condition can be solved. It would be an intuitive solution to solve this if-condition on CPU, i.e. before line 8 of the Alg. 2 so as to skip

the whole calling of GPU. However, in such a case, the CPU needs to have knowledge about previously computed segments, which means that the value of the lineal path function has to be sent to CPU for every segment separately inside the for-loop before line 18. Our computations, however, revealed that repeated sending of one integer from GPU to CPU is time-consuming and it is faster to call repeatedly the GPU, solve the if-condition there (i.e. before line 10) and store all the computed values of the lineal path function only on GPU until the last segment is computed. Then sending of the whole vector of the lineal path values brings significant time savings. This latter variant was implemented and is further called as *enhanced*, while the original version of the algorithm without any algorithmic acceleration is called *standard*.

The performance of GPU parallelism is demonstrated on evaluation of the L_2 -function on three different microstructures: (i) chess-type morphology with dimensions of squares 10×10 [px], (ii) particulate suspension consisting of equal-sized squares with dimensions 4×4 [px] and (iii) metal foam taken from [22]. Tab. 1 compares the amount of time necessary averaged over five evaluations of the lineal path function for both phases on single CPU or GPU devices depending on the image size and chosen variant of the algorithm. In particular, the computational times correspond to a part of the lineal path function computation, which is called repeatedly within the optimisation process, i.e. evaluation of lines 1 to 5 in Alg. 2 is excluded. It is shown that for very small images the use of CPU outperforms the GPU because of additional time spent by communicating with the GPU. Nevertheless, for images of 50×50 [px] the GPU achieves an evident speed-up which mostly further increases with the increasing dimensions of the image. The exception is the chess-type microstructure where a specific phase distribution limits the length of the most of the line segments to 10 [px]. This significantly elevates the acceleration obtained for the enhanced variant of the algorithm and even the CPU version is so fast that communication with GPU leads again to deceleration which increases with the image dimensions.

| | | | | | | | |
|---|----------------------|----------------------|---------------------|----------------------|----------------------|---------------------|----------------------|
|  | <i>Standard</i> | | | <i>Enhanced</i> | | | |
| dim. [px] | GPU [s] | CPU [s] | S [—] | GPU [s] | CPU [s] | S [—] | S^* [—] |
| 10×10 | $2.4 \cdot 10^{-3}$ | $0.59 \cdot 10^{-3}$ | 0.2 \times | $2.4 \cdot 10^{-3}$ | $0.39 \cdot 10^{-3}$ | 0.2 \times | 0.2 \times |
| 20×20 | $11.9 \cdot 10^{-3}$ | $11.9 \cdot 10^{-3}$ | 1.0 \times | $11.1 \cdot 10^{-3}$ | $7.8 \cdot 10^{-3}$ | 0.7 \times | 1.1 \times |
| 50×50 | 0.15 | 0.55 | 3.7 \times | 0.10 | 0.24 | 2.5 \times | 5.8 \times |
| 100×100 | 2.1 | 7.0 | 3.3 \times | 0.26 | 0.27 | 1.0 \times | 27.0 \times |
| 200×200 | 32.6 | 110.9 | 3.4 \times | 2.0 | 1.0 | 0.5 \times | 53.9 \times |
| 500×500 | 318.4 | 1071.1 | 3.4 \times | 16.3 | 6.4 | 0.4 \times | 65.8 \times |

| | | | | | | | |
|---|----------------------|----------------------|---------------------|----------------------|----------------------|---------------------|----------------------|
|  | <i>Standard</i> | | | <i>Enhanced</i> | | | |
| dim. [px] | GPU [s] | CPU [s] | S [—] | GPU [s] | CPU [s] | S [—] | S^* [—] |
| 10×10 | $2.5 \cdot 10^{-3}$ | $0.71 \cdot 10^{-3}$ | 0.3 \times | $2.5 \cdot 10^{-3}$ | $0.38 \cdot 10^{-3}$ | 0.2 \times | 0.3 \times |
| 20×20 | $12.9 \cdot 10^{-3}$ | $16.0 \cdot 10^{-3}$ | 1.2 \times | $12.5 \cdot 10^{-3}$ | $8.2 \cdot 10^{-3}$ | 0.7 \times | 1.3 \times |
| 50×50 | 0.16 | 0.81 | 5.0 \times | 0.13 | 0.36 | 2.7 \times | 6.0 \times |
| 100×100 | 2.5 | 16.1 | 6.4 \times | 1.7 | 7.2 | 4.1 \times | 9.3 \times |
| 200×200 | 41.9 | 256.3 | 6.1 \times | 20.8 | 78.0 | 3.7 \times | 12.3 \times |
| 500×500 | 411.6 | 2544.0 | 6.2 \times | 205.1 | 789.1 | 3.9 \times | 12.4 \times |

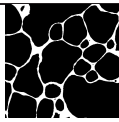
| | | | | | | | |
|---|----------------------|----------------------|----------------------|----------------------|----------------------|---------------------|----------------------|
|  | <i>Standard</i> | | | <i>Enhanced</i> | | | |
| dim. [px] | GPU [s] | CPU [s] | S [—] | GPU [s] | CPU [s] | S [—] | S^* [—] |
| 10×10 | $2.4 \cdot 10^{-3}$ | $0.73 \cdot 10^{-3}$ | 0.3 \times | $2.4 \cdot 10^{-3}$ | $0.65 \cdot 10^{-3}$ | 0.3 \times | 0.3 \times |
| 20×20 | $12.0 \cdot 10^{-3}$ | $13.8 \cdot 10^{-3}$ | 1.1 \times | $11.9 \cdot 10^{-3}$ | $9.7 \cdot 10^{-3}$ | 0.8 \times | 1.2 \times |
| 50×50 | 0.17 | 1.31 | 7.6 \times | 0.15 | 0.67 | 4.4 \times | 8.7 \times |
| 100×100 | 2.8 | 31.9 | 11.5 \times | 2.22 | 17.2 | 7.7 \times | 14.3 \times |
| 200×200 | 48.3 | 577.9 | 12.0 \times | 32.9 | 241.7 | 7.3 \times | 17.5 \times |
| 500×500 | 542.1 | 7911.7 | 14.6 \times | 445.2.1 | 3884.2 | 8.7 \times | 17.7 \times |

Table 1: Comparison of CPU and GPU performance averaged over five evaluations (S stands for speedup and S^* represents overall speedup obtained by hardware and software acceleration)

The particular computations presented in Tab. 1 were performed on 2× INTEL Xeon E5 – 2620 @ 2.0 GHz, 96 GB RAM, 2× GPU - NVIDIA QUADRO 4000 with Microsoft Windows 7 64-bit operating system and the CUDA v. 6.5. Furthermore, the algorithm is also designed for dual GPUs, unfortunately scalability towards the multiple GPU devices is not considered here. The logical step for the dual GPU algorithm is to uniformly distribute the generated segments, so that each device holds only a certain amount of them. This improvement thus results in lower memory requirements.

4. Optimisation procedure

Before proceeding to the comparative study of the lineal path and two-point probability function, we briefly describe the optimisation procedure employed in our computations. Here, we used the framework firstly introduced by Yeong and Torquato [10] for digitised media. The algorithm is based on simulated annealing method independently developed by Kirkpatrick et al. [23] and Černý [24]. It starts with some randomly generated microstructure and quantification of its quality by a chosen statistical descriptor. The microstructure is then modified by a chosen operator and its new quality is evaluated. The acceptance of the proposed modification is governed by the Metropolis rule, which allows with a certain probability to accept a worse solution and thus to escape from a local extreme. Such a generic optimisation scheme opens the possibility to define modification operator suitable for a given microstructure. For instance, a particulate suspension consisting of equal-sized discs can be modified by moving a centre of an arbitrarily chosen disc, see e.g. [7, 8]. Such a move affects the whole set of pixels and allows preserving the known shape of particles, thus accelerating the optimisation procedure. Most of the microstructures are, however, not consisting of particles having a specific known shape. Then the simplest modification operator is based on interchanging two randomly chosen pixels from different phases, which at least allows to preserve their volume fraction [10]. Very simple acceleration employed in our implementation consists in a random selection of interfacial pixels which leads to a significant increase of accepted modifications, as presented in [25].

Since the proposed way of porting the lineal path evaluation onto GPU counts with copying the whole image from CPU to GPU for any new proposed modification, the modification operator can be designed in any convenient way. Nevertheless, our further computations use solely the interchanging of

| |
|---|
| <pre> Data: binary image with dimensions $W \times H$ Result: optimised SEPUC corresponding to given image 1 <i>create_random_image</i>(P); 2 $SDP = \text{evaluate}(P)$; 3 $T = T_{\max}$; 4 $T_{\text{mult}} = (T_{\min}/T_{\max})^{(\text{succ}_{\max}/N_{\text{step}})}$; 5 while $c < N_{\text{step}}$ do 6 $c = s = 0$; 7 while $c < c_{\max}$ & $s < s_{\max}$ do 8 $c = c + 1$; 9 $Q = \text{modify}(P)$; 10 $SDQ = \text{evaluate}(Q)$; 11 if <i>random_number</i> $U[0,1] < \exp((SDQ - SDP)/T)$ then 12 $s = s + 1$; 13 $P = Q$; 14 $SDP = SDQ$; 15 end 16 end 17 $T = T \cdot T_{\text{mult}}$; 18 end </pre> |
|---|

Algorithm 3: Algorithmic structure of simulated annealing

two pixels. The particular structure of the employed optimisation algorithm is given in Alg. 3. First of all, a random digitised image P is created with the same volume fractions of phases as the original morphology. Its statistical similarity to the original image is then evaluated using the chosen statistical descriptor SD as the least square error:

$$e(\text{SD}^i) = \sum_{p \in \mathbb{D}} (\text{SD}_{\text{original}}^i(\mathbf{x}_p) - \text{SD}^i(\mathbf{x}_p))^2, \quad (19)$$

where the superscript i denotes the phase for which the SD is evaluated and the subscript p corresponds to the component of a discretised descriptor. If the superscript i is missing in the following text, the SD is evaluated for both phases. Note that the least square error in Eq. (19) also consists of a large number of simple arithmetic operations, which are again efficiently evaluated in parallel on GPU.

$$\begin{aligned} N_{\text{step}} &= 4 \cdot 10^6 & c_{\text{max}} &= 0.1 N_{\text{step}} \\ T_{\text{min}} &= 0.01 T_{\text{max}} & s_{\text{max}} &= 0.01 N_{\text{step}} \end{aligned}$$

Table 2: Control parameters of simulated annealing method

Control parameters of the algorithm were set to following values: The value of T_{max} was manually changed for every particular computation so as to achieve approximately the ration $s/c = 0.5$ within the first few steps of the algorithm. Some other recommendations for setting these parameters can be found e.g. in [26].

5. Microstructure reconstruction

Reconstruction of a microstructure from its statistical description is an inverse problem addressed by several authors in different ways, see [25, 27, 28] and the references therein. Here we follow the concept proposed in [10], where the discretised randomly generated microstructure is optimised with respect to the prescribed statistical descriptor. The authors in [29] presented numerical evidence that a periodic medium discretised into pixels is completely specified by its two-point correlation function, up to a translation and, in some cases, inversion. This conclusion implies that the reconstruction pro-

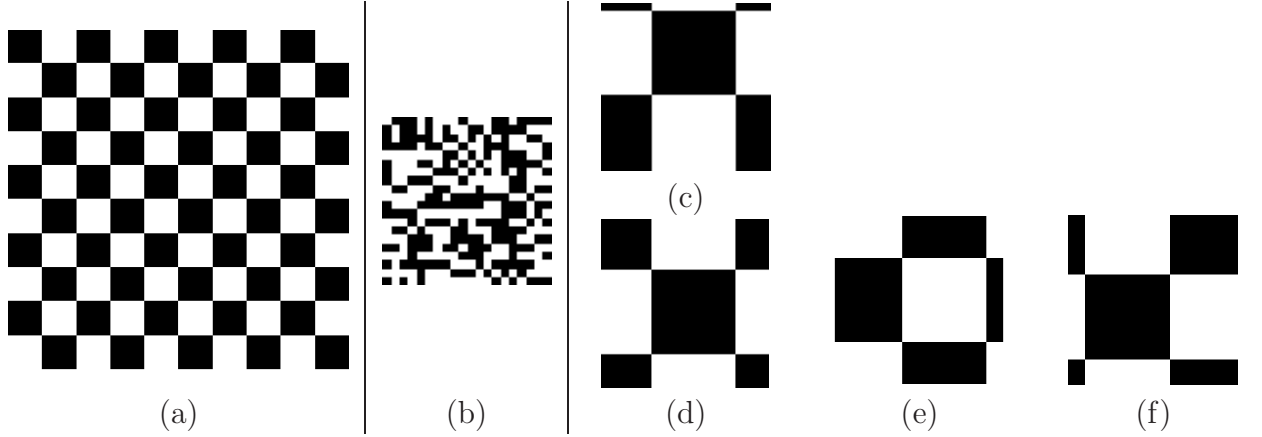
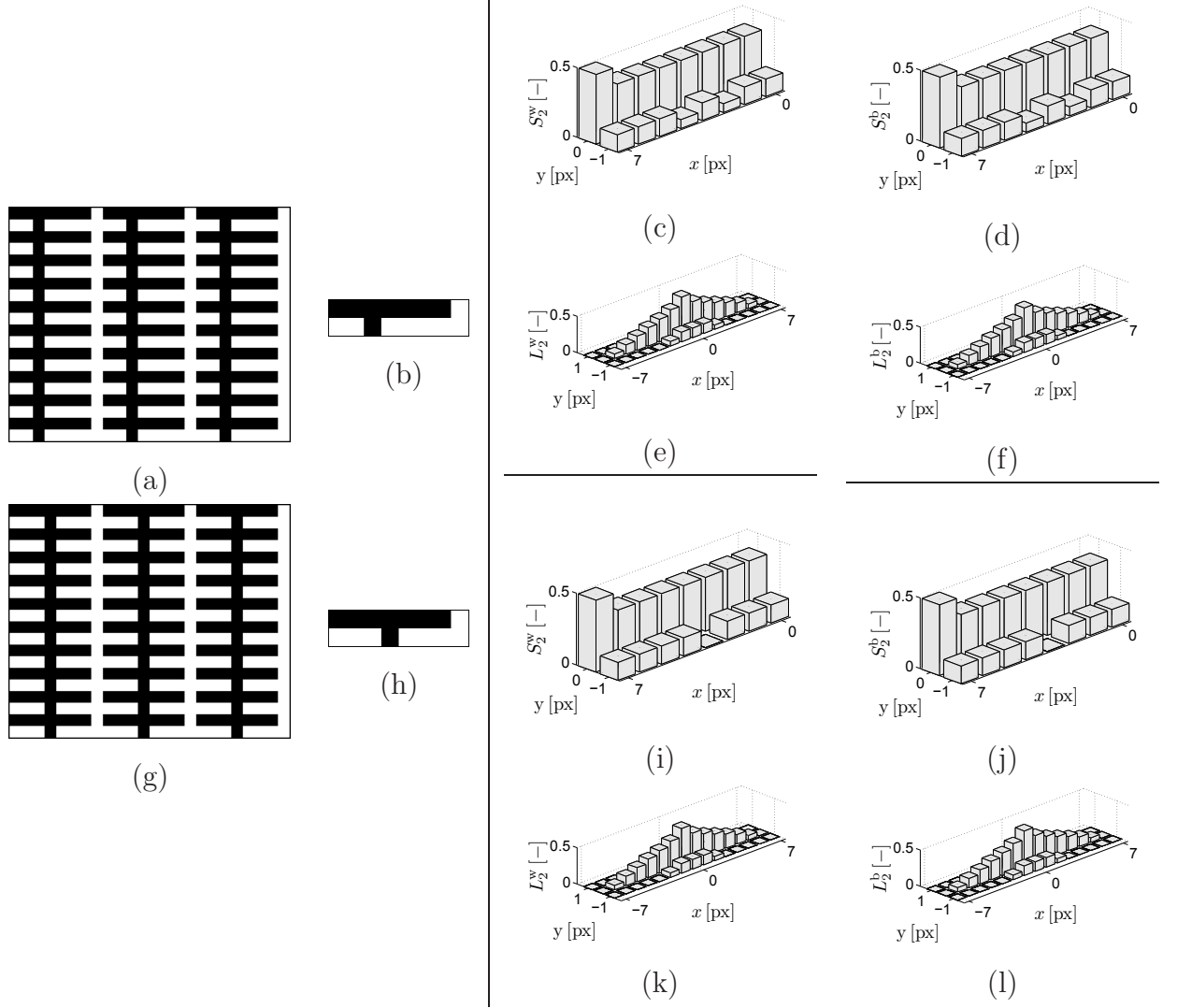


Figure 10: Chess microstructure: (a) Original medium with size 100×100 [px] and characteristic lengths 20×20 [px]; (b) Random initial structure, size 20×20 [px]; (c) S_2 -based reconstructed image; (d) L_2 -based reconstructed image; (e) L_2^b -based reconstructed image; (f) L_2^w -based reconstructed image; obtained within less than $5 \cdot 10^5$ iterations.

cess based on the discretised two-point probability function has a unique solution. For many microstructural morphologies, the same holds also for



reconstruction from the lineal path function. For instance, the chess-type morphology is fully defined not only by lineal path function computed for both phases, but only one of the phase is fully sufficient to completely define the morphology, see Figure 10. Nevertheless, generic evidence for a unique solution of the lineal path function-based reconstruction is missing and is suggested just by findings concerning orientation-dependent chord length distributions in continuous domains [30]. On the contrary, we can demonstrate that employing Bresenham’s algorithm for the line segments’ definition, the lineal path function does not define a unique solution for a reconstruction process based on a discretised medium.

Fig. 11 shows an example of two different periodic cells of dimensions 2×8 pixels. Due to the same volume fraction of both phases, the two-point probability functions obtained for both phases in Fig. 11c-d are identical, which is in agreement with the Eq. 5, but both functions differ from the corresponding ones obtained for the other cell in Fig. 11i-j. The lineal path functions are, on the other hand, identical for both phases in Fig. 11e-f as well as for both phases obtained for the second cell in Fig. 11k-l. This proves a non-unique solution of a reconstruction process for the chosen highly rough discretisation. Of course, for a higher resolution, the difference between the lineal path function obtained for both cells can be again revealed. As a conclusion, the reconstruction process based on the discretised medium has always a unique solution in case of the two-point probability function and also mostly in case of the lineal path function where the differences among a potential set of solutions are decreasing with increasing resolution.

Based on this conclusion, we can proceed to the comparison of the entire lineal path function L_2 with its Monte Carlo-based approximation \tilde{L}_2 within the reconstruction process. Considering the microstructures depicted in Fig. 7, we may assume that their reconstruction based on the entire lineal path function will lead to almost the same microstructures as the original ones in case of the microstructures B and C and to exactly same one in case of A. To decrease computational demands of the comparison, we reduced the dimensions of the microstructures to 50×50 pixels. The reconstruction process is driven again as the minimisation of the least square error given in Eq. 14. The Monte Carlo-based approximation – described in Sec. 3 – is applied here to evaluate both the lineal path functions of the original as well as of the reconstructed image, respectively. In order to investigate the influence of the approximation quality, we have considered three levels corresponding to the Monte Carlo evaluation based on $N = 10, 100$ and 1000 samples. The

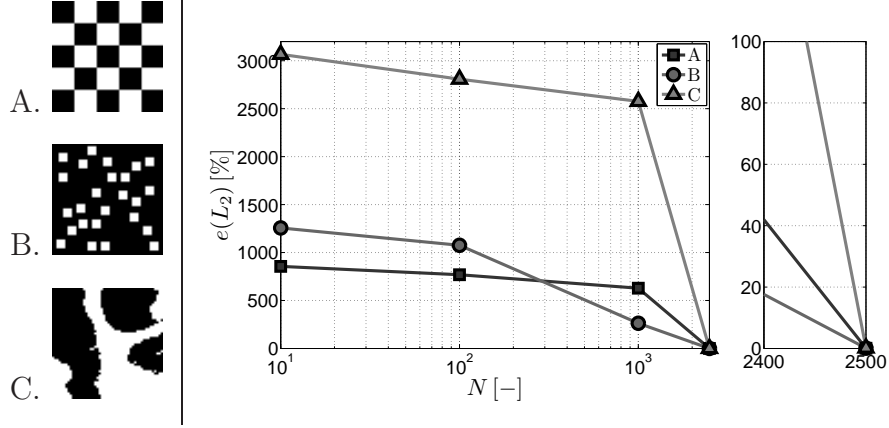


Figure 12: Comparison of the entire L_2 and its approximation \tilde{L}_2 used in microstructure reconstruction for different values of N

results are compared with the reconstruction based on the entire lineal path function, where the number of samples is identical with the number of pixels in the images, i.e. $N = 2500$.

The relative errors of the final reconstructed L_2 -based images related to the entire lineal path function L_2 of original images are displayed in Fig. 12. The displayed values reveal that the reconstruction procedure based on the lineal path approximation converges very slowly with the number of evaluated samples and the reconstruction process thus leads to images with the lineal path function, which is highly different from the prescribed one.

6. Microstructure compression

While the reconstruction process aims at rediscovering of a microstructure with dimensions and spatial statistics defined by the given descriptor, the compression process tries to reduce the information content of the given morphology and searches for its compressed representation by a small statistically similar periodic cell [5, 31] or a set of compatible cells [7]. After evaluating a chosen statistical descriptor over the whole available domain of the original medium, one needs to decide about the cells' dimensions and accordingly cut the dimensions of the descriptor. Then the compression process proceeds in an exactly same manner as the microstructure reconstruction.

As our numerical implementations of the two-point probability function

and the lineal path function are both based on the assumption of periodicity, they will not provide precise results when applied to original random and non-periodic microstructure. Nevertheless, as already mentioned previously, in [18] it was shown that the assumption of periodicity does not introduce a systematic bias in the values of the descriptors.

6.1. Particulate suspension

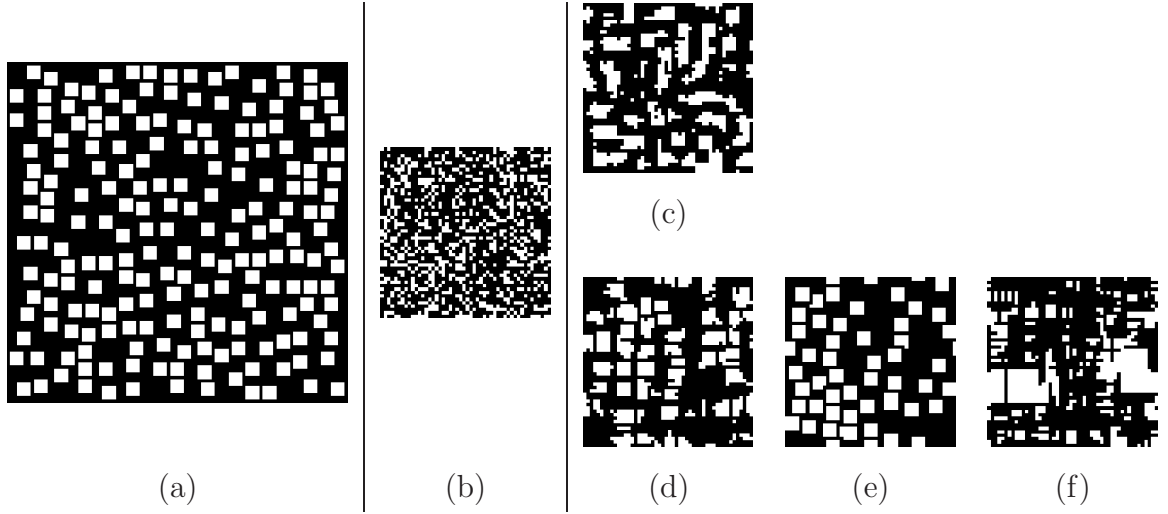


Figure 13: Particulate suspension: (a) Original medium, size 100×100 [px], particles 4×4 [px]; (b) Random initial structure, size 50×50 [px]; (c) Compressed S_2 -based image, size 50×50 [px]; (d) Compressed L_2^b and L_2^w -based image, size 50×50 [px]; (e) Compressed L_2^w -based image, size 50×50 [px]; (f) Compressed L_2^b -based image, size 50×50 [px]

The first example comparing properties of the S_2 - and L_2 -based compression concerns an artificially created particulate suspension consisting of equal-sized white squares randomly distributed within a black matrix, see Fig. 13. The shape of particles is a very significant property of such a microstructure, which can be easily preserved by modifying the optimisation algorithm so as to start with randomly distributed particles and then to move their centres within the optimisation process. Nevertheless, here we aimed at testing the descriptors in their ability to capture such an important property within the compression process.

Fig. 13c shows that the S_2 -based compression leads to significant deterioration of the shape of particles. This is caused by the very small ratio of

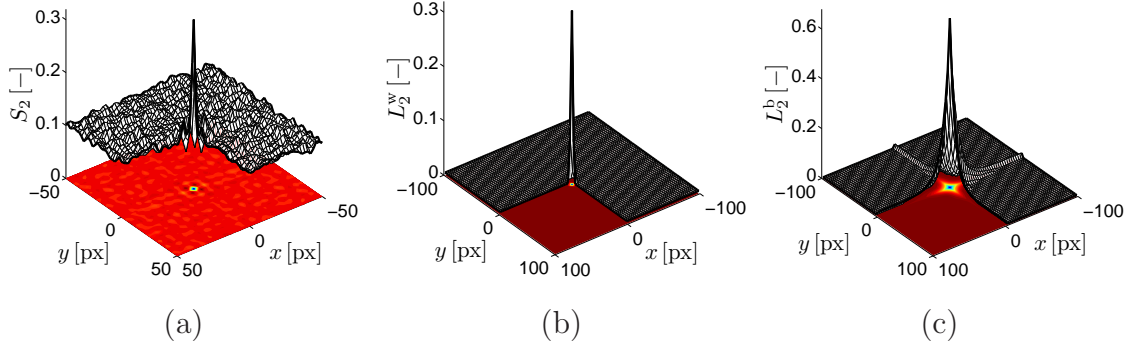


Figure 14: Particulate suspension: (a) Original medium, size 100×100 [px], particles 4×4 [px]; (b) S_2 -function; (c) L_2^w -function; (d) L_2^b -function

the particles over the size of the PUC, i.e. 4×4 [px] vs. 50×50 [px]. The information about their shape is thus saved on a small portion of the descriptor's domain corresponding to short-range correlations (see Fig. 14a), while the most of the domain defines long-range correlations corresponding to the mutual distances of the particles. The lineal path function allows to separate the information about the shape of particles and their mutual positions, since the L_2^w in Fig. 14b contains only the first, while the L_2^b in Fig. 14c defines mostly the latter. According to that, the L_2^w -based compression in Fig. 13e leads obviously to the well compressed shape of particles, while the L_2^b -based compression in Fig. 13f does not capture the shape of particles at all and the L_2 -based compression in Fig. 13d provides a compromise solution. It is hard to evaluate the quality of obtained structures in an objective manner, but we can conclude that the L_2 function allows a user to emphasise short-range effects as needed.

Another interesting aspect concerns the mutual comparison of the compressed microstructures and the corresponding errors in describing original medium according to Eq. (14), which are listed in Tab. 3. While the optimisation of S_2 leads to a microstructure which is relatively good also with respect to L_2 and comparable with microstructures obtained for the L_2^w - or L_2^b -based optimisation, the opposite is not true. The microstructures optimised w.r.t. one or both phases of L_2 manifest very bad correlations, which are comparable or even worse than those obtained for a random image. The lineal path

function thus cannot be applied for a correlations-based compression.

| Compressed medium | $e(S_2)$ | $e(L_2)$ |
|-------------------------|----------------------|----------------------|
| Random Fig. 13b | $3.12 \cdot 10^{-1}$ | $1.68 \cdot 10^1$ |
| S_2 -based Fig. 13c | $9.20 \cdot 10^{-3}$ | $2.35 \cdot 10^0$ |
| L_2 -based Fig. 13d | $3.09 \cdot 10^{-1}$ | $2.73 \cdot 10^{-2}$ |
| L_2^w -based Fig. 13e | $3.53 \cdot 10^{-1}$ | $1.08 \cdot 10^0$ |
| L_2^b -based Fig. 13f | $6.52 \cdot 10^{-1}$ | $9.60 \cdot 10^{-1}$ |

Table 3: Mutual comparison of compressed microstructures.

6.2. Epithelial cells

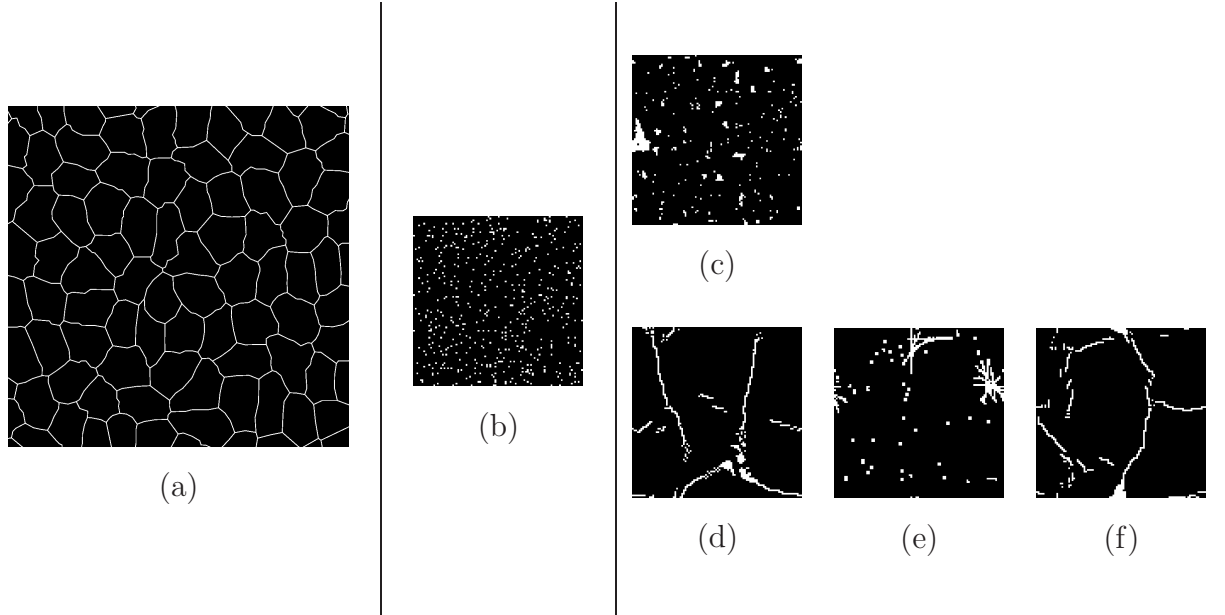


Figure 15: Epithelial cells: (a) Original medium, size 510×510 [px]; (b) Random initial structure, size 100×100 [px]; (c) Compressed S_2 -based image, size 100×100 [px]; (d) Compressed L_2^b and L_2^w -based image, size 100×100 [px]; (e) Compressed L_2^w -based image, size 100×100 [px]; (f) Compressed L_2^b -based image, size 100×100 [px]

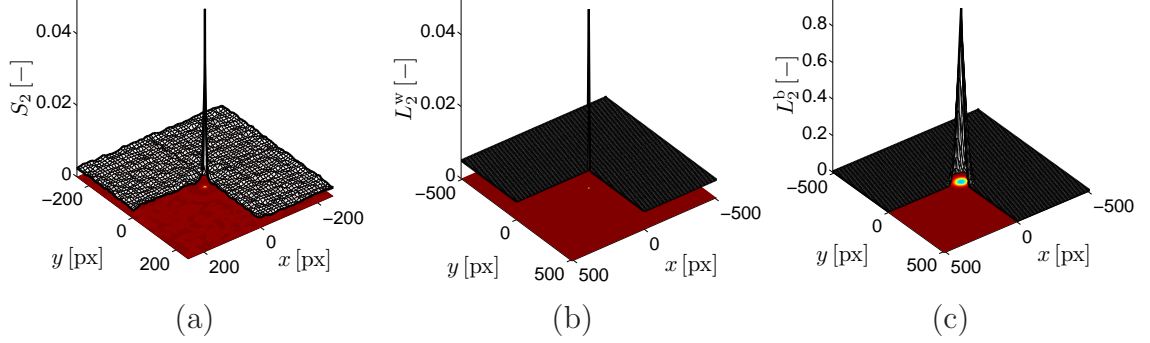


Figure 16: Epithelial cells: (a) Original medium, size 100×100 [px]; (b) S_2 -function; (c) L_2^w -function; (d) L_2^b -function

Epithelial cells are a typical example of morphology characterised by very thin and continuous walls, see Fig. 15a. Their volume fraction is very small, only 4.97 [%] and thickness is mostly equal to only 1 pixel. The assembling of continuous walls from random initial arrangement is rather unattainable. As can be expected, the two-point probability function fails completely in this task, see Fig. 15c. Nevertheless, the assumption that the continuity of the white walls can be captured by the lineal path computed for the white phase is wrong. As a matter of fact, the nonlinear walls are composed of a set of short line segments and the L_2^w -based compression thus leads to their random stars-resembling arrangement as visible in Fig. 15e. The continuity of walls is actually closely related to cells, whose limited size requires the continuity of the surrounding medium. As a consequence, the information about the continuity of walls is surprisingly hidden in L_2^b , see results of L_2^b -based compression in Fig. 15f. Due the small volume fraction of the white phase, its influence on the L_2 -based compression is rather small and the results are principally similar to the L_2^b -based compression, cf. Figs. 15d and 15f. The remaining discontinuities are very difficult to be improved within the proposed optimisation strategy based on random interchanging of two pixels. We can only assume that the full connectivity of walls can be obtained using some more sophisticated modification operator.

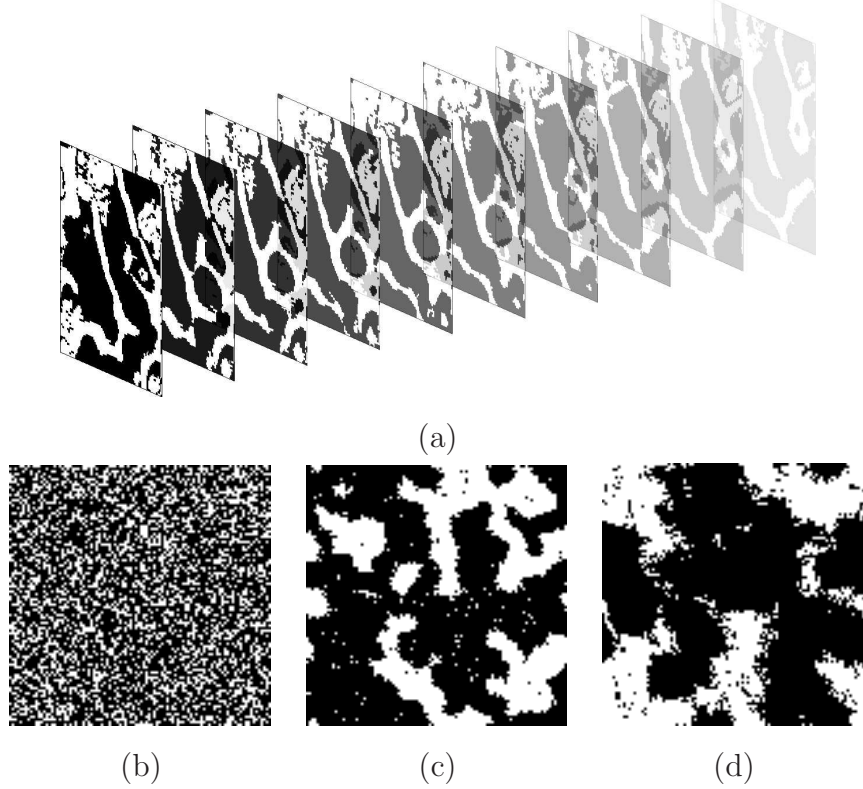


Figure 17: Trabecular bone microstructure obtained by micro Computed Tomography [32]: (a) 3-D cuts of original structure, 100×100 [px]; (b) Initial random morphology corresponding to volume fraction ϕ^b and ϕ^w of original medium, 100×100 [px]; (c) Compressed S_2 -based structure, 100×100 [px]; (d) Compressed L_2 -based structure, 100×100 [px]

6.3. Trabecular bone

The last example concerns trabecular bone, which represents a medium with approximately equal volume fractions of both phases creating continuous irregular branches. Our original microstructural specimen consists of $100 \times 100 \times 100$ [px] three-dimensional image obtained by micro Computed Tomography [32]. We divide this data into ensemble of 100 two-dimensional cuts 100×100 [px] and by employing the assumption of ergodicity, the statistical descriptors are computed as an average over the ensemble. The computational effort in case of the L_2 -based reconstruction is enormous. Although the part of the L_2 calculation was ported to GPU, the whole compression process for image 100×100 [px] lasted days, recall Tab. 1 for time require-

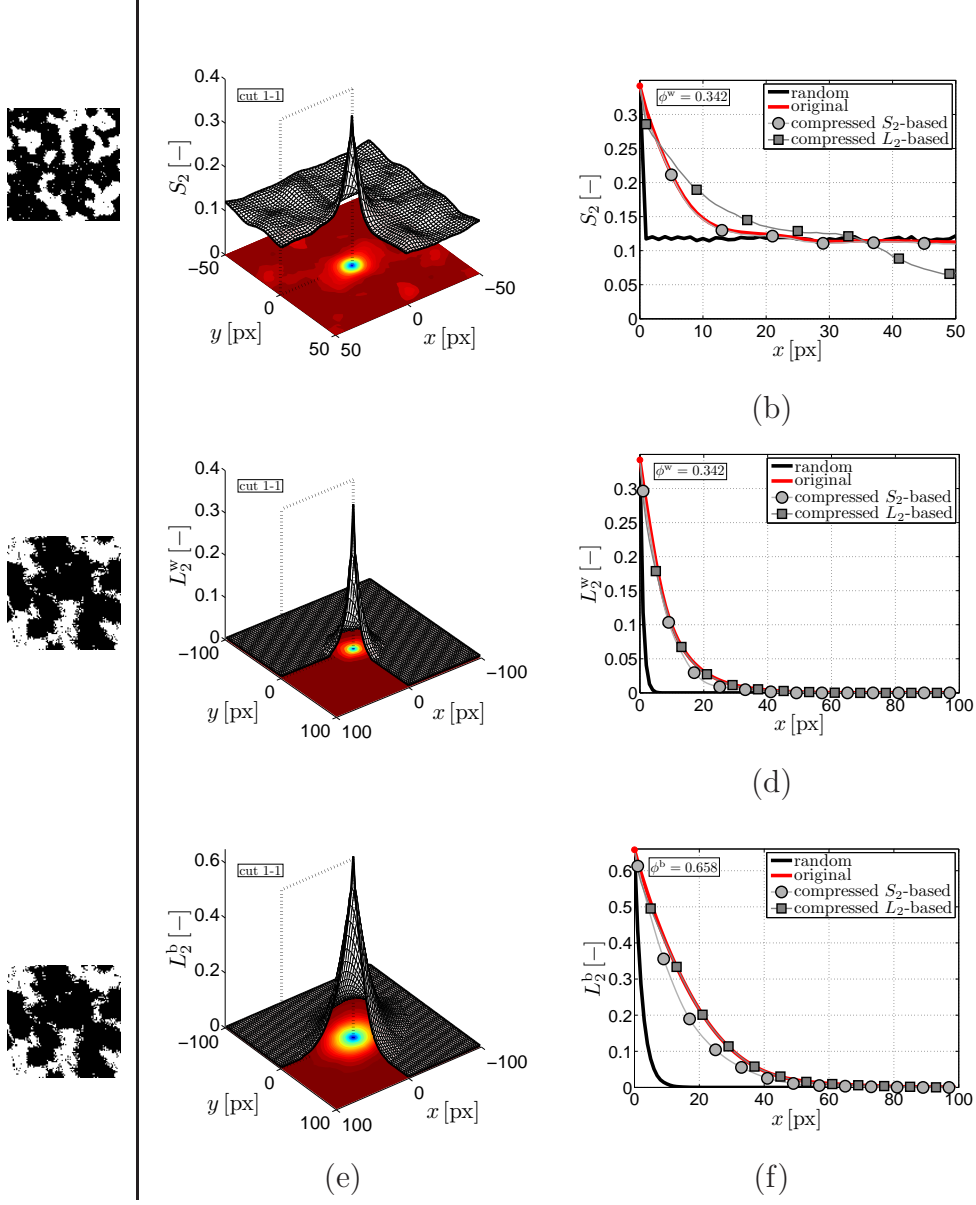


Figure 18: Results of compressed trabecular bone microstructure: (a) S_2 -function of compressed S_2 -based medium; (b) Comparison of S_2 -functions in cut 1-1; (c) L_2^w -function of compressed L_2 -based system; (d) Comparison of L_2^w -functions in cut 1-1; (e) L_2^b -function of compressed L_2 -based system; (f) Comparison of L_2^b -functions in cut 1-1;

ments of the single L_2 evaluation. According to relations in Sec. 2, the overall number of operations for single standard calculation² of the L_2^i -function is $6.716 \cdot 10^9$ comparing to $1.021 \cdot 10^5$ operations of the S_2 evaluation.

The final compressed S_2 and L_2 -based structures are shown in Figs. 17c and d, respectively. The S_2 - and L_2 -functions of original and new microstructures are then summarised in Fig. 18. It is clearly visible that the optimised functions very well coincide with the prescribed ones, see Fig. 18b,d,f. However, the same does not hold for a microstructure optimised w.r.t. one descriptor, but then evaluated w.r.t. to other. The L_2 -based compressed microstructure manifests much stronger short-range correlations, see Fig. 18b, while the S_2 -based compressed microstructure underestimates the connectivity and, especially in the black phase, consists of a smaller number of continuous line segments, see Fig. 18f. Nevertheless, we can conclude that both descriptors provide visually well compressed microstructures and even the two-point probability function allows to obtain continuous regions similar to the original medium.

7. Conclusions

The paper is devoted to comparison of the lineal path function and the two-point probability function in reconstruction and compression of two-phase microstructures. So as to investigate properties of the descriptors in a sufficient detail and to avoid some misleading conclusions based on rough discretisation of the lineal path by an approximately evaluated sampling template, the accelerated version of the entire lineal path function was proposed. The acceleration involves namely reformulation of the sequential C/C++ code for the repeatedly called part of the lineal path function into the parallel C/C++ code with CUDA extensions enabling the use of computational potential of the NVIDIA graphics processing unit (GPU). Even though the algorithm requires to copy relatively large data structures to the GPU, it was shown that the principal limitations reside in computational time required within the compression or reconstruction process, where the lineal path function needs to be often called more than million times. Despite the parallel

²The number of operations related to enhanced version of L_2^i evaluation cannot be determined exactly because of missing knowledge about zero segments. However, it is approximately 97 percent less operations for dimensions 100×100 [px], i.e. approximately $2.0 \cdot 10^8$ operations.

evaluation of the lineal path function on GPU, the evaluation of the two-point probability function remains faster even on a single CPU thanks to its accelerated formulation based on the Fast Fourier Transform.

The accelerated discrete versions of both descriptors were successfully employed for microstructure reconstruction and compression processes governed by the simulated annealing algorithm based on interchanging of two interfacial pixels belonging to opposite phases. It was demonstrated that unlike the two-point probability function, the discrete version of the lineal path function based on line segments defined by Bresenham's algorithm does not generally ensure a unique solution of a reconstruction process. Nevertheless, the difference among the feasible solutions is small and decreases with the increasing resolution. On the other hand, many different morphologies could be fully defined by the lineal path computed for only one continuous phase.

Three particular microstructures were employed for illustration of typical features of both descriptors. The particulate suspension consisting of equal sized squares revealed incapability of the S_2 function to capture the shape of particles, which can be emphasised by the L_2 function. Example of epithelial cells demonstrated that very thin walls also cannot be captured by the S_2 function and that the computation of L_2 corresponding to the phase of walls is surprisingly not needed to achieve the mostly connected walls in the compressed cell. Trabecular bone, on the other hand, represents an example of mutually penetrating phases of comparable volume fractions, where both descriptors provided visually well looking microstructures.

We may conclude that despite the proposed acceleration steps, the lineal path function remains computationally expensive descriptor, which can be, however, essential for compression of morphologies consisting of specific formations such as particles or thin walls.

Acknowledgment

This outcome has been achieved with the financial support of the Czech Science Foundation, projects No. 105/12/1146, No. 105/11/P370 and No. 13-24027S. We would like to thank Ondřej Jiroušek of Institute of Theoretical and Applied Mechanics, Czech Republic for providing us the measured image data of microstructures and Jan Zeman of Czech Technical University, Czech Republic, for bringing our attention to coupling the spatial statistics with GPU computations.

References

- [1] S. Torquato, Random Heterogeneous Materials: Microstructure and Macroscopic Properties, Springer; Corrected edition, 2006.
- [2] J. Vorel, M. Šejnoha, Evaluation of homogenized thermal conductivities of imperfect carbon-carbon textile composites using the Mori-Tanaka method, *Structural Engineering and Mechanics* 33 (2009) 429–446.
- [3] J. Sýkora, T. Krejčí, J. Kruis, M. Šejnoha, Computational homogenization of non-stationary transport processes in masonry structures, *Journal of Computational and Applied Mathematics* 18 (2012) 4745–4755.
- [4] J. Sýkora, M. Šejnoha, J. Šejnoha, Homogenization of coupled heat and moisture transport in masonry structures including interfaces, *Applied Mathematics and Computation* 219 (13) (2013) 7275–7285.
- [5] J. Zeman, M. Šejnoha, From random microstructures to representative volume elements, *Modelling and Simulation in Materials Science and Engineering* 15 (4) (2007) 325–335.
- [6] J. Schröder, D. Balzani, D. Brands, Approximation of random microstructures by periodic statistically similar representative volume elements based on lineal-path functions, *Archive of Applied Mechanics* 81 (7) (2011) 975–997.
- [7] J. Novák, A. Kučerová, J. Zeman, Compressing random microstructures via stochastic wang tilings, *Physical Review E* 86 (4) (2012) 040104.
- [8] J. Novák, A. Kučerová, J. Zeman, Microstructural enrichment functions based on stochastic wang tilings, *Modelling and Simulation in Materials Science and Engineering* 21 (2) (2013) 025014.
- [9] M. Doškář, J. Novák, J. Zeman, Aperiodic compression and reconstruction of real-world material systems based on Wang tiles, *Physical Review E* 90 (2014) 062118.
- [10] C. L. Y. Yeong, S. Torquato, Reconstructing random media, *Physical Review E* 57 (1998) 495–506.

- [11] G. L. Povirk, Incorporation of microstructural information into models of two-phase materials, *Acta Metallurgica et Materialia* 43 (8) (1995) 3199 – 3206.
- [12] D. S. Li, M. A. Tschopp, M. Khaleel, X. Sun, Comparison of reconstructed spatial microstructure images using different statistical descriptors, *Computational Materials Science* 51 (1) (2012) 437–444.
- [13] H. Singh, A. M. Gokhale, S. I. Lieberman, S. Tamirisakandala, Image based computations of lineal path probability distributions for microstructure representation, *Materials Science and Engineering A* 474 (1-2) (2008) 104–111.
- [14] J. Zeman, Analysis of composite materials with random microstructure, Ph.D. thesis, Klokner Institute, Czech Technical University in Prague (2003).
- [15] E. Kröner, Bounds for effective elastic moduli of disordered materials, *Journal of the Mechanics and Physics of Solid* 25 (1977) 137–155.
- [16] M. J. Beran, Statistical continuum theories, *Monographs in Statistical Physics*, Interscience Publishers, 1968.
- [17] M. Lombardo, J. Zeman, M. Šejnoha, G. Falsone, Stochastic modeling of chaotic masonry via mesostructural characterization, *International Journal for Multiscale Computational Engineering* 7 (2) (2009) 171–185.
- [18] J. Gajdošík, J. Zeman, M. Šejnoha, Qualitative analysis of fiber composite microstructure: Influence of boundary conditions, *Probabilistic Engineering Mechanics* 21 (4) (2006) 317–329.
- [19] B. Lu, S. Torquato, Lineal-path function for random heterogeneous materials, *Physical Review A* 45 (2) (1992) 922–929.
- [20] J. E. Bresenham, Algorithm for computer control of a digital plotter, *IBM System journal* 4 (1) (1965) 25–30.
- [21] NVIDIA corporation (www), <http://developer.nvidia.com/page/home.html>, accessed: 2015-02-23.

- [22] O. Jiroušek, T. Doktor, D. Kytýř, P. Zlámal, T. Fíla, P. Koudelka, I. Jandajsek, X-ray and finite element analysis of deformation response of closed-cell metal foam subjected to compressive loading, *Journal of Instrumentation* 8 (2) (2013) 2012–2016.
- [23] S. Kirkpatrick, C. D. Gelatt, M. P. Vecchi, Optimization by simulated annealing, *Science* 220 (4598) (1983) 671–680.
- [24] V. Černý, Thermodynamical approach to the traveling salesman problem: An efficient simulation algorithm, *Journal of Optimization Theory and Applications* 45 (1) (1985) 41–51.
- [25] M. G. Rozman, M. Utz, Efficient reconstruction of multiphase morphologies from correlation functions, *Physical Review E* 63 (6) (2001) 066701.
- [26] M. Lepš, M. Šejnoha, New approach to optimization of reinforced concrete beams., *Computers & Structures* 81 (18–19) (2003) 1957–1966.
- [27] P. Čapek, V. Hejtmánek, L. Brabec, A. Zikánová, M. Kočířík, Stochastic reconstruction of particulate media using simulated annealing: Improving pore connectivity, *Transport in Porous Media* 76 (2) (2009) 178–198.
- [28] M. A. Davis, S. D. C. Walsh, M. O. Saar, Statistically reconstructing continuous isotropic and anisotropic two-phase media while preserving macroscopic material properties, *Physical Review E* 83 (2011) 026706.
- [29] M. G. Rozman, M. Utz, Uniqueness of reconstruction of multiphase morphologies from two-point correlation functions, *Physical Review Letters* 89 (13) (2002) 135501.
- [30] W. Nagel, Orientation-dependent chord length distributions characterize convex polygons, *Journal of Applied Probability* 30 (3) (1993) 730–736.
- [31] H. Lee, M. Brandyberry, A. Tudor, K. Matouš, Three-dimensional reconstruction of statistically optimal unit cells of polydisperse particulate composites from microtomography, *Physical Review E* 80 (2009) 061301.
- [32] O. Jiroušek, P. Zlámal, D. Kytýř, M. Kroupa, Strain analysis of trabecular bone using time-resolved X-ray microtomography, *Nuclear Instruments and Methods in Physics Research Section A: Accelerators,*

Spectrometers, Detectors and Associated Equipment 663 (2011) S148–S151.